

Progress Towards Accurate Monitoring of Flue Gas Emissions

Aaron Johnson¹, Iosif Shinder, Michael Moldover, Joey Boyd, James Filla
Sensor Science Division, NIST, Gaithersburg, MD 20899

Abstract

The amounts of CO₂ and other pollutants emitted by a coal-fired power plant are measured using a continuous emissions monitoring system (CEMS) permanently installed in the exhaust smokestack. The pollutant flux is the product of the pollutant's concentration and the flow in the stack. The concentration measurements are traceable to certified reference standards; however, the complex velocity fields (i.e., swirling flow with a skewed velocity profile) in stacks make accurate flow measurements difficult. Therefore, the CEMS flow monitor, which commonly consists of a single-path ultrasonic flow meter, must be calibrated at least once a year by a procedure called a relative accuracy test audit (RATA). This calibration is generally performed using a differential pressure probe called an S-type pitot probe. However, S-probes are not accurate when used in complex velocity fields. NIST developed a 1/10th scale-model smokestack simulator (SMSS) to quantify the uncertainty of diverse stack flow measurement techniques. The SMSS generates complex, stack-like flows, but with an expanded uncertainty (95 % confidence level) in the average velocity of 0.7 %. Using the SMSS, we assessed S-probe-based RATAs and both single and two-crossing-path (X-pattern) CEMS ultrasonic flow monitors. Remarkably, the X-pattern ultrasonic CEMS deviated by only 0.5 % from the NIST's flow standard. In contrast, a single-path ultrasonic CEMS deviated from NIST standards by 14 % to 17 % in a highly distorted flow. Deviations for the S-probe RATAs ranged from 5 % to 6 %.

1 Introduction

The combustion gases from coal-fired power plants (CFPPs) are exhausted into vertical, large diameter ($D_{\text{stack}} > 5$ m) smokestacks. These stacks disperse combustion gases high in the atmosphere to minimize pollution at the ground level. To quantify the amount of pollutants released into the atmosphere, the total flow in the stack must be accurately measured. However, stacks, are not designed to facilitate accurate flow measurements. The network of elbows, reducers, fans, etc. upstream of the stack inlet generate complex velocity fields that make accurate stack flow measurements difficult. Additional difficulties occur because the flue gas from CFPPs is hot (around 50 °C), saturated with water vapor, and depleted in oxygen (asphyxiating). Despite the difficulties, pollutant emissions are measured by Continuous Emissions Monitoring Systems (CEMS) installed in these smokestacks.

CEMS systems measure both the concentration and the total flow in the stack. The product of the concentration and the total flow is the instantaneous rate of pollutant efflux. Since 1992 NIST² has supported accurate CEMS concentration measurements by providing certified gas mixtures called NIST Traceable Reference Materials (NTRMs) to the stack testing community [1]. These NTRMs are traceable to NIST primary standards at specified uncertainty levels, and are often used as standards to verify the accuracy of stack concentration measurements [2 - 5]. Before the present work, NIST

¹ Corresponding Author: aaron.johnson@nist.gov

² The National Institute of Standards and Technology (NIST) is the U.S. National Metrology Institute.

was not involved in establishing standards for accurate stack flow measurements. Yet, the flow measurement is arguably more significant than the concentration measurement. An erroneous measurement of the concentration of a pollutant affects the mass calculation of that one pollutant, while an erroneous flow measurement is multiplied by all the concentration measurements and therefore leads to erroneous values of *all* emitted pollutants. Furthermore, *all* of the pollutant values are biased in the same direction as the erroneous flow measurement.

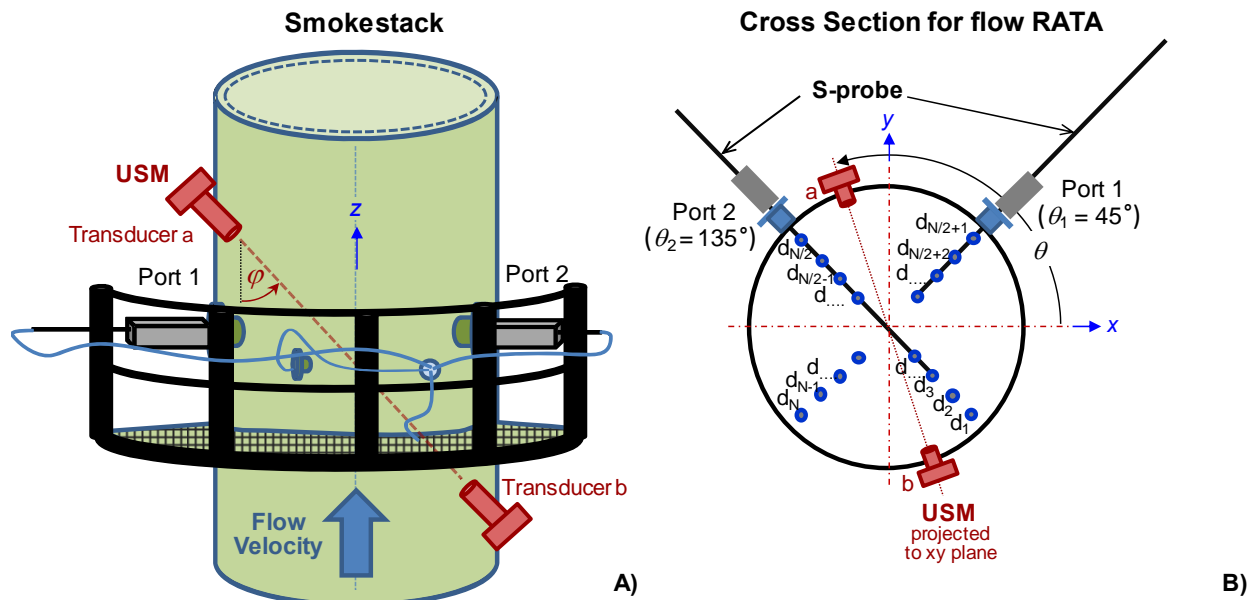


Figure 1. Sketch of catwalk surrounding a smokestack with installed apparatus for measuring the flow in the smokestack. A) single-path Ultrasonic Flow Monitor (USM) installed at path angle φ , and two orthogonal ports (Port 1 and Port 2) used for the flow RATA, and B) stack cross section showing locations $d_1 \dots d_N$ where axial flow velocities are measured by traversing an S-probe through ports 1 and 2. In this figure θ denotes the installation angle of the two ports and of the USM.

In CFPPs the most widely used CEMS flow monitor is a single-path ultrasonic flow meter (USM) [6]. Figure 1 depicts a single-path USM installed in a stack at a path angle φ and at an installation angle of θ . The axial flow velocity is determined using the expression

$$\bar{V}_{USM,f} = k \bar{V}_{USM,p} / \cos \varphi, \quad (1)$$

where k is the experimental (or theoretical) calibration factor; and the bar above the velocity “ $\bar{}$ ” denotes that the velocity is the average value over the path. As such, $\bar{V}_{USM,p}$ is the path-averaged velocity directed along the acoustic path indicated by the dashed line in Fig. 1A³. This velocity is determined by measuring the time it takes ultrasonic pulses to travel the distance between transducers a and b with and against the flow. If the transit times are accurately measured and the path length (L_p) is known, $\bar{V}_{USM,p}$ can be accurately determined. However, the velocity that is essential for accurate emissions measurements is $\bar{V}_{USM,f}$, which is directed along the stack axis.

³ Throughout this document USM quantities with the subscript “p” indicate the value of that quantity along the acoustic path (L_p is the path length, a_p is average sound speed along the path, etc.). The subscript “f” is used to denote the USM velocity directed along the stack axis (*i.e.*, the flow velocity).

Unfortunately, $\bar{V}_{\text{USM},f}$ cannot in general be accurately determined by a single path USM. For stack flows, the uncertainty of an uncalibrated single path USM typically ranges from 5 % to 20 %. The cause of this error is two-fold. First, the geometric factor $1/\cos\phi$ in Eq. (1) is intended to convert the velocity directed along the acoustic path to the velocity along the stack axis. However, if the cross-flow velocity (V_c), commonly called swirl, is not zero, then the resulting velocity is not directed along the stack axis and is therefore not indicative of the flow velocity. Second, the USM only provides a path-averaged velocity instead of the area weighted velocity required to determine the average flow. The difference between the path and area weighted velocity can be substantial when the axial velocity profile is not non-uniform. We herein refer to this error as a profile effect. Because stack flows have complex velocity fields with non-zero cross-flows and asymmetric velocity profiles, the swirl and profile effect errors of single path USMs are generally too large to provide sufficient accuracy for emission measurements. To improve CEMS flow measurement accuracy, the USMs are calibrated at least yearly by an EPA protocol called a relative accuracy test audit (RATA). This RATA generally uses an S-type pitot probe to measure the axial velocity at prescribed locations along the cross section of a stack [7 - 9]. Figure 1B illustrates how an S-type pitot probe is inserted into the stack access ports and traversed along the 2 orthogonal chords to the prescribed measurement locations. The velocity measurements made at points d_1 . . . d_N are area-weighted to determine the average flow velocity, which is subsequently used to determine the calibration factor k in Eq. (1).

Although current regulations require CEMS flow measurements to be calibrated against the flow RATA, this correction does not necessarily improve the flow measurement accuracy. The accuracy of the S-probe, like the USM, degrades in the complex velocity fields inherent to stack flows. The S-probe's accuracy degrades because this probe is only designed to measure 2 components of the velocity vector. Researchers have shown that when the third component of velocity (*i.e.*, the velocity along the pitch angle) differs between calibration and application, large errors can result [10, 11]. In stack applications, S-probes are calibrated in a wind tunnel at zero pitch angle, but are used in stacks where a typical pitch angle ranges from $-10^\circ \leq \alpha \leq 10^\circ$. More extreme pitch angles are possible, depending on the piping configuration and flow conditions immediately upstream of the stack inlet. Shinder showed that when a calibrated S-probe is used at large negative pitch angles (*e.g.*, $\alpha = -10^\circ$) errors can exceed 6 % [10]. Moreover, many flow RATAs are performed using uncalibrated S-probes, which can introduce errors of 10 % or more [12, 13].

Flow RATA errors are transferred to CEMS flow measurements and can result in unknown biases in stack flow measurements. In this work, we assess the accuracy of an X-pattern USM. The single-path USM in Fig. 1 can be converted to the X-pattern design by installing a second USM at the same path angle ($\phi_2 = \phi_1$) and spaced 180° apart from the first USM ($\theta_2 = \theta_1 + 180^\circ$). The X-pattern is shown in Fig. 6. The X-pattern flow velocity is defined as the arithmetic average of the flow velocities of the 2 single-path USMs. To avoid introducing a potential bias from the S-probe flow RATA we did not flow calibrate the X-pattern or the single path USM in this research (*i.e.*, $k = 1$ in Eq. (1)). We assessed the absolute accuracy of these uncalibrated CEMS in smokestack-like flow conditions using a facility called the Scale-Model Smokestack Simulator (SMSS) [14]. Remarkably, we found average velocity measured by the X-pattern CEMS was within 1 % of the NIST traceable reference velocity in the SMSS facility. In contrast, the accuracy of a single-path USM ranged from 5 % to 17 % depending

on its θ orientation. The accuracy of the S-probe RATA ranged from 5 % to 6 % depending on the number of traverse points, flow conditions, and θ orientation.

This manuscript documents the performance of CEMS and RATA flow measurements in NIST's SMSS facility. Section 2 describes the SMSS, which generates smokestack-like flow conditions in a 1.2 m diameter Test Section, but measures the flow with an expanded uncertainty (corresponding to a 95 % confidence level) of 0.7 % using a reference meter traceable to NIST primary flow standards. Section 3 describes the RATA method; Section 4 gives a physical explanation why the X-pattern CEMS compensates for swirl and a single path USM does not; Section 5 presents the results of an S-probe RATA, a single path USM, and the X-pattern CEMS tested in the SMSS facility; and Section 6 states our conclusions.

2 Scale-Model Smokestack Simulator (SMSS)

NIST designed and built the Scale-Model Smokestack Simulator (SMSS) shown in Figs. 2 and 3. The SMSS is used to 1) assess the flow measurement accuracy of the Relative Accuracy Test Audit (RATA), 2) quantify the performance of Continuous Emissions Measurement Systems (CEMS) flow monitors, and 3) serve as a testbed for new stack flow measurement techniques. In this work, we used the SMSS to evaluate the performance of the S-probe RATA, single-path CEMS flow monitor, and X-pattern CEMS flow monitor. Because stack flow measurements depend primarily on the characteristics of the velocity field, and not on the gas composition, the SMSS uses air as a surrogate for flue gas. In its Test Section ($D_{\text{test}} = 1.2$ m diameter), the SMSS generates complex velocity fields (*i.e.*, turbulent, swirling flow, with an asymmetric velocity profile) prevalent in industrial-scale stacks.



Figure 2. Scale-Model Smokestack Simulator (SMSS) showing the sections where air enters and exits the facility. RATA and CEMS performance evaluation are performed inside the building in its 1.2 m diameter Test Section.

Air enters the SMSS at the Air Intake Unit shown in Fig. 2. In the Test Section, the average air flow velocity ranges from 5 m/s to 26 m/s; this range spans the velocities in industrial scale CFPPs stacks. The unique feature of the SMSS is that the average flow velocity (V_{NIST}), is traceable to NIST's primary flow standards and known to 0.7 % expanded uncertainty [14, 15]. Therefore, the SMSS can assess the *absolute accuracy* of CEMS flow monitors. In contrast, typical RATA measurements can assess only the *relative accuracy* of CEMS systems because they rely on S-probes that are often not calibrated and that do not account for the complexity of the flow field.

The schematic diagram shown in Fig. 3 highlights the functional design of the SMSS facility. Quiescent air is drawn into the air intake unit by fans at the facility exit. Cross-flow velocity components are damped as air moves through the intake unit. Low-speed air exiting the intake unit accelerates through a cone (Fig. 1) and establishes a low-swirl, nearly-uniform velocity profile in the Reference Section. We measure the flow in the Reference Section using a NIST-calibrated, 8 path ultrasonic flow meter (USM) [15]. Because the velocity field in the Reference Section is practically free of flow distortions, a high accuracy flow measurement is straightforward. We point out, however, that the 8 path USM can accurately measure the flow even when the flow has significant levels of swirl and asymmetry [16, 17].

In contrast, to the distortion-free flow in the Reference Section, the velocity field in the Test Section is designed to replicate the complex velocity fields typical to stack flows. Flow distortions in an industrial scale smokestack are caused by fans, reducers, and most notably a sharp corner where the flue gas enters the stack. In a similar manner, flow distortions in the SMSS Test Section result from the sharp corner shown in Fig. 3.

The leaks in the SMSS are negligible; therefore, the air flux in the Test and Reference Sections are equal. The NIST-traceable flow measurement in the Reference Section determines the average flow velocity (V_{NIST}) in the Test Section by accounting for the diameter and gas density changes between the sections. V_{NIST} is used to assess the performance of CEMS flow monitors and the flow RATA.

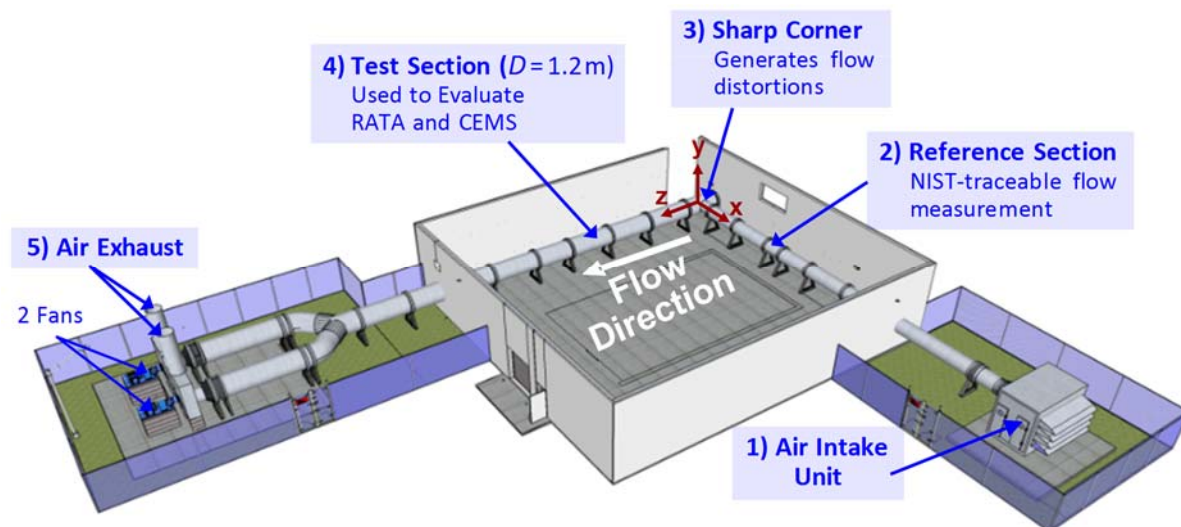


Figure 3. Schematic of the 5 sections of the SMSS facility. 1) air enters the intake unit, 2) a well-conditioned flow is measured in the Reference Section using a NIST-traceable flow meter, 3) sharp corner generates swirling, asymmetric flow, 4) Test Section used for assessing the accuracy of RATA and CEMS in distorted flows, and 5) fans that drive the flow and exhaust it to the atmosphere.

3 S-probe RATA Methodology

We conducted an S-probe RATA 12 diameters (14.4 m) downstream of the sharp corner shown in Fig. 3. During setup, an S-probe was installed in the SMSS Test Section with its positive pressure port aligned with the pipe centerline (*i.e.*, the z-axis in Fig. 3). The axial velocities were measured at $2N$ points along the two orthogonal chords shown in Fig. 1B. In accordance with EPA

Method 2 [9], the N points on each chord were spaced at the centroids of equal area so that the flow velocity measured by the S-probe is

$$V_{\text{Sprobe}} = \sum_{n=1}^{2N} w_n V_{\text{Sprobe},n} \quad , \quad (2)$$

where the weighting factor is $w_n = 1/2N$, and the S-probe velocity measured at each n^{th} point is deduced from the Bernoulli equation [18]

$$V_{\text{Sprobe},n} = C_p \sqrt{2 \Delta P_n / \rho} \cos(\beta_{\text{FLOW},n}) \quad , \quad (3)$$

where $C_p = 0.84$ is the value of the S-probe calibration factor conventionally used in the stack testing community. In Eq. (3), ρ is the average air density in the RATA cross section; it is determined to better than 0.2 % using an equation of state [19] that depends on the measured pressure, temperature, and relative humidity. The flow angle is $\beta_{\text{FLOW},n}$ and ΔP_n is the measured differential pressure with the S-probe oriented at the flow angle. As illustrated in Fig. 4, the flow angle is determined by first rotating the probe to the yaw-null angle ($\beta_{\text{NULL},n}$) where $\Delta P_n = 0$, and then rotating the S-probe 90° in the negative yaw angle direction.

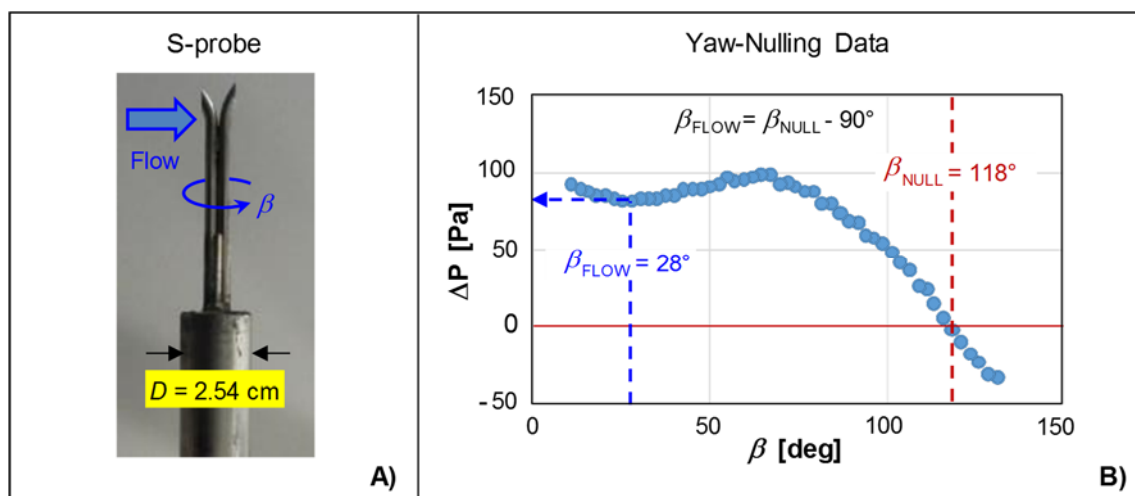


Figure 4. S-probe yaw-nulling method: A) S-probe showing the direction positive yaw angle rotation (β), and B) measurements of the differential pressures (ΔP) across S-probe ports as a function of β . The null angle (β_{NULL}) is characterized by $\Delta P = 0$ and β_{FLOW} is 90° from β_{NULL} .

4 CEMS Measurements

We made flow measurements using 3 single-path USMs installed 10 diameters downstream from the sharp corner in Fig. 3. All 3 USMs were installed in the same flow meter body shown in Fig. 5A. Figures 5B, 5C, and 5D show the orientation of each path in the meter body. Path 1 is vertically oriented at a 45° angle relative to the Test Section's centerline while Paths 2 and 3 are oriented horizontally at a 45° angle relative to the centerline. The linear distance between the transducers is the path length (L_p), and the orientation of the path relative to the pipe centerline is the path angle (φ). In industrial CFFP stacks, L_p and φ are not always accurately measured. Instead, the flow RATA

calibration corrects 1) for biases attributed to CEMS dimensional errors and 2) for flow related biases attributed to the complex stack velocity field. Since the goal of this work is to assess the absolute accuracy of a single-path and the X-pattern USM, we used a laser tracking system to measure L_p 's and ϕ 's with expanded uncertainties of 0.25 % and 0.5 °. The uncertainties of these dimensional measurements are negligible relative to flow related uncertainties attributed to profile and swirl effects; therefore, differences between the average velocity measured by the single path and X-pattern relative to the NIST standard velocity can be ascribed to flow related errors.

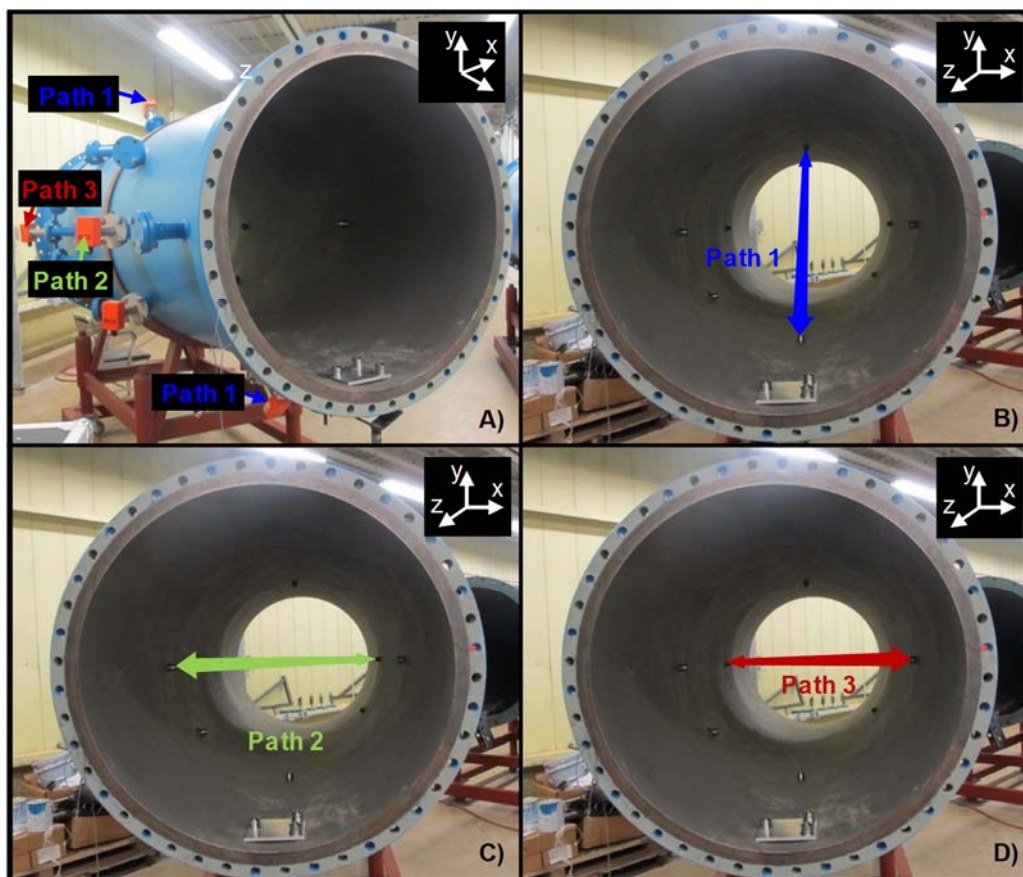


Figure 5. Three single-path USMs installed in the same spool located $10 D_{test}$ downstream of sharp corner in Fig. 3: A) Three transmitting/receiving transducers of the USMs on the pipe exterior. B), C), and D) are interior views of the 3 paths used by the 3 transducer pairs. Paths 2 and 3 together comprise an X-pattern USM.

4.1 USM Principle of Operation

Industrial USMs used in stack applications measure the time it takes an ultrasonic pulse to travel the distance L_p . Two distinct time measurements are necessary to determine the flow velocity. The 2 times are denoted t_w and t_a , respectively, where t_w is the time it takes an ultrasonic pulse to travel L_p *with* (or assisted by the flue gas velocity) and t_a is the time required for another pulse to travel L_p moving *against* (or retarded by the velocity of the flue gas). If a_p and $\bar{V}_{USM,p}$ are the respective speed of sound along the acoustic path and path velocity, then the two measured times are 1) $t_w = L_p / (a_p + \bar{V}_{USM,p})$ and 2) $t_a = L_p / (a_p - \bar{V}_{USM,p})$. When the flow along the path moves in the same

direction as the ultrasonic pulse, the pulse moves at the sound speed augmented by $\bar{V}_{USM,p}$. Likewise, when the fluid moves opposite to the pulse, the pulse speed is the sound velocity reduced by $\bar{V}_{USM,p}$. Solving these two equations for the path velocity gives

$$\bar{V}_{USM,p} = \frac{L_p}{2} \left(\frac{1}{t_w} - \frac{1}{t_a} \right). \tag{4}$$

For low speed flows ($M_p < 0.1$) where $M_p = V_p/a_p$ is the Mach number, Eq. (4) is accurate to the order M_p^2 . Given that most stack flows satisfy this Mach number criterion, USMs can typically measure $\bar{V}_{USM,p}$ to better than 0.5 %, provided L_p is known, and the USM signal processing is sufficiently robust to accurately measure t_a and t_w . However, the bulk flow is determined by the component of velocity along the stack axis, not by $\bar{V}_{USM,p}$. Common practice is to estimate the axial velocity by dividing $\bar{V}_{USM,p}$ by $\cos(\varphi)$ as shown in Eq. (1). This approximate formulation accurately predicts the flow velocity only when the magnitude of the cross-flow velocity (V_c) is small relative to the axial flow and profile effects are negligible. If V_c is significant relative to the flow velocity, $\bar{V}_{USM,p}$ will consist of velocity components from flow along the stack axis (V_z), but also from the cross flow (V_c). That is, V_c will influence the transit time of an ultrasonic pulse moving from the emitting to the receiving transducers. Since stack flows usually have significant swirl levels, single-path USMs generally do not provide accurate flow measurements. In contrast, the X-pattern design compensates for swirl-related errors.

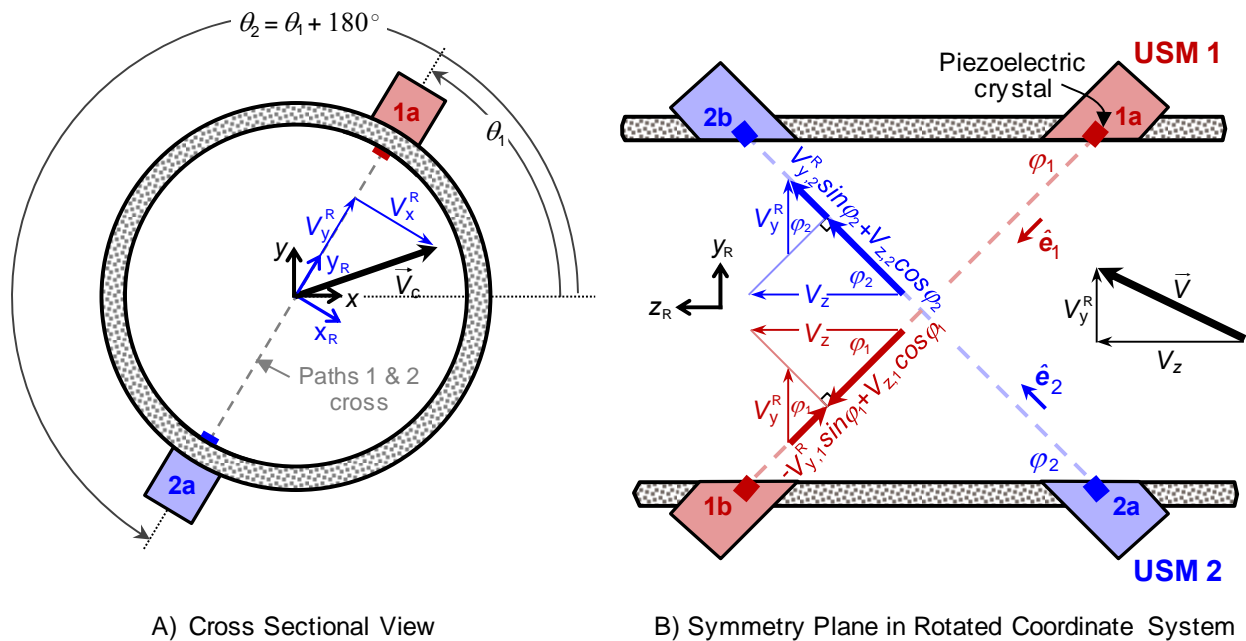


Figure 6. Sketch showing 2 single-path USMs 1 and 2, which together comprise the X-pattern configuration. A) cross-sectional view displaying USM installation angles θ_1 and θ_2 , and cross-flow velocity \vec{V}_c in 2 coordinate frames (x, y) and (x_R, y_R) , and B) shows a symmetry plane in rotated coordinates where the velocities along paths 1 and 2 have contributions both from the axial and cross-flow components of the fluid velocity (\vec{V}).

4.2 X-pattern Swirl Compensation

An X-pattern consists of the two USMs 1 and 2 installed in the same plane with opposite orientations (in Fig. 6A, $\theta_2 = \theta_1 + 180^\circ$.) and with the same path angle, $\varphi_1 = \varphi_2$. Here, we show that perfect compensation for swirl (*i.e.*, the non-axial velocity components) occurs only where the two ultrasonic beams cross on the axis of the stack at $y_R = 0$. At other y_R locations the swirl cancelation is not perfect; however, extensive empirical evidence has shown the X-pattern does an excellent job compensating for swirl [20]. We give an intuitive picture and a physical explanation on why the X-pattern USM provides superior swirl compensation relative to the currently used single path USM.

Figure 6 shows an orthographic drawing of an X-pattern USM. In this example, the fluid velocity vector is $\vec{V} = V_z \vec{k} + \vec{V}_c$ where V_z is the axial velocity, and \vec{V}_c is the cross-flow velocity vector that generates swirl errors. Figure 6A shows the components of \vec{V}_c in the coordinate frame (x_R, y_R, z_R) rotated about the z-axis so that V_x^R is orthogonal to acoustic paths 1 and 2, and does not influence the USM transit time measurements. In the rotated reference frame, the acoustic path trajectories are described solely by the coordinates y_R and z_R as illustrated in Fig. 6B. Therefore, the travel times of an ultrasonic pulse moving along paths 1 or 2 are dependent only on the cross-flow velocity V_y^R and on the axial velocity V_z . Summing the contributions from both velocity components gives the following average velocity along path 1

$$\bar{V}_{\text{USM,p1}} = \bar{V}_{z,1} \cos \varphi_1 - \bar{V}_{y,1}^R \sin \varphi_1 \quad (5a)$$

where $\bar{V}_{z,1}$ and $\bar{V}_{y,1}^R$ are the average axial and cross-flow velocities along path 1. Likewise, the average velocity along path 2 is

$$\bar{V}_{\text{USM,p2}} = \bar{V}_{z,2} \cos \varphi_2 + \bar{V}_{y,2}^R \sin \varphi_2 \quad (5b)$$

where $\bar{V}_{z,2}$ is the average axial flow velocity along the path and $\bar{V}_{y,2}^R$ is the average cross-flow velocity along path 2⁴. Due to the orientation of paths 1 and 2 a positive cross-flow velocity reduces the speed on path 1, but increases the speed on path 2. Using Eq. (1) to calculate the flow velocity on these paths leads to

$$\bar{V}_{\text{USM,f1}} = \frac{\bar{V}_{\text{USM,p1}}}{\cos \varphi_1} = \bar{V}_{z,1} - \bar{V}_{y,1}^R \tan \varphi_1 \quad (6a)$$

for path 1 and

$$\bar{V}_{\text{USM,f2}} = \frac{\bar{V}_{\text{USM,p2}}}{\cos \varphi_2} = \bar{V}_{z,2} + \bar{V}_{y,2}^R \tan \varphi_2, \quad (6b)$$

⁴ Equations (6a) and (6b) can also be developed taking the dot product of the fluid velocity vector with the unit tangent vectors \hat{e}_1 and \hat{e}_2 , respectively: $\bar{V}_{\text{USM,p1}} = \vec{V} \cdot \hat{e}_1$ and $\bar{V}_{\text{USM,p2}} = \vec{V} \cdot \hat{e}_2$ where based on the geometry in Fig. 6B

$\hat{e}_1 = -\sin \varphi_1 \hat{e}_y^R + \cos \varphi_1 \hat{k}$ and $\hat{e}_2 = \sin \varphi_2 \hat{e}_y^R + \cos \varphi_2 \hat{k}$ and the unit vector in the y_R direction is $\hat{e}_y^R = \cos \theta_1 \hat{i} + \sin \theta_1 \hat{j}$.

for path 2. These equations illustrate how the cross-flow velocities $\bar{V}_{y,1}^R$ and $\bar{V}_{y,2}^R$ cause errors in the performance of single-path USMs. The flow velocity of USM 1 is decreased by $\bar{V}_{y,1}^R \tan \varphi_1$ while it is increased by $\bar{V}_{y,2}^R \tan \varphi_2$ for USM 2. Since the X-pattern is the arithmetic average of USM 1 and 2 its flow velocity is given by

$$\bar{V}_{\text{USMX},f} \approx \frac{\bar{V}_{z,1} + \bar{V}_{z,2}}{2} \quad (6c)$$

where the term $(\bar{V}_{y,2}^R \tan \varphi_2 - \bar{V}_{y,1}^R \tan \varphi_1)/2$ has been omitted from Eq. (6c) since its value is nearly zero. The X-pattern path angles are the same ($\varphi_2 = \varphi_1$), and the average velocities along each path tend to be of the same sign and magnitude ($\bar{V}_{y,2}^R \approx \bar{V}_{y,1}^R$).

Swirl is dissipated by viscous shear caused by the no-slip condition at the pipe wall. For high Reynolds number (Re) flows like the SMSS ($Re = 4.7 \times 10^5$ to 2.0×10^6) and CFPPs stacks ($Re = 2.4 \times 10^6$ to 2.6×10^7), experiments show that swirl effects can persist for 100 pipe diameters or more [21, 22]. In contrast, the axial distance between paths 1 and 2 of the X-pattern in Fig. 6B is less than one pipe diameter ($z_{R2} - z_{R1} < D_{\text{test}}$) at any fixed value of y_R . The local cross-flow velocity at a fixed value of y_R is $V_{y,1}^R(x_R, y_R, z_{R1})$ at path 1 and $V_{y,2}^R(x_R, y_R, z_{R2})$ at path 2. Since swirl requires many pipe diameters to dissipate, the local cross-flow velocities are nearly equal on acoustic paths 1 and 2, $V_{y,1}^R(x_R, y_R, z_{R1}) \approx V_{y,2}^R(x_R, y_R, z_{R2})$. Consequently, the average cross-flow velocities are also nearly equal, $\bar{V}_{y,2}^R \approx \bar{V}_{y,1}^R$. Therefore, the X-pattern compensates for swirl errors and generally outperforms the single-path USM. The effectiveness of the X-pattern to dissipate swirl has been empirically and computationally verified by numerous researchers [20, 23-25].

5 Results from the SMSS

5.1 Velocity Profile and Cross Flow in SMSS Test Section

We used an S-probe to measure the normalized axial velocity profile ($V_{\text{Sprobe},n}/V_{\text{NIST}}$) and the flow angle (β_{FLOW}) along two orthogonal chords in the SMSS Test Section. Measurements were made at $z = 12 D_{\text{test}}$ where z the axis centerline originating at the coordinate system located at the sharp corner shown in Fig. 3. We measured the axial velocity and flow angle along the chords oriented at $\theta_1 = 45^\circ$ and at $\theta_2 = 135^\circ$ using a custom designed automated traversing system (ATS) [14]. Figure 1B shows the orientation of the two traverse chords relative to the xy -coordinate axes. Although the figure shows two S-probes simultaneously traversing the cross section, the ATS (not shown) only has one access port. Once the S-probe is installed into this access port the ATS rotates the pipe section containing the S-probe about the z -axis to the specified θ orientations. At each θ orientation, the traverse system moves the probe across the chord to the prescribed traverse points. At each point, the ATS rotates the S-probe about its axis to find β_{NULL} and β_{FLOW} . The traverse distance at any point on the chord is defined by the parameter ξ , which is zero at the inner pipe wall (i.e., the wall closest to the ATS access port) and D at the outer pipe wall (farthest from the ATS

assess port). We measured $V_{\text{Sprobe},n}/V_{\text{NIST}}$ and β_{FLOW} at 24 points located at the centroids of equal area on each chord. At each point the S-probe velocity is determined using Eq. (3).

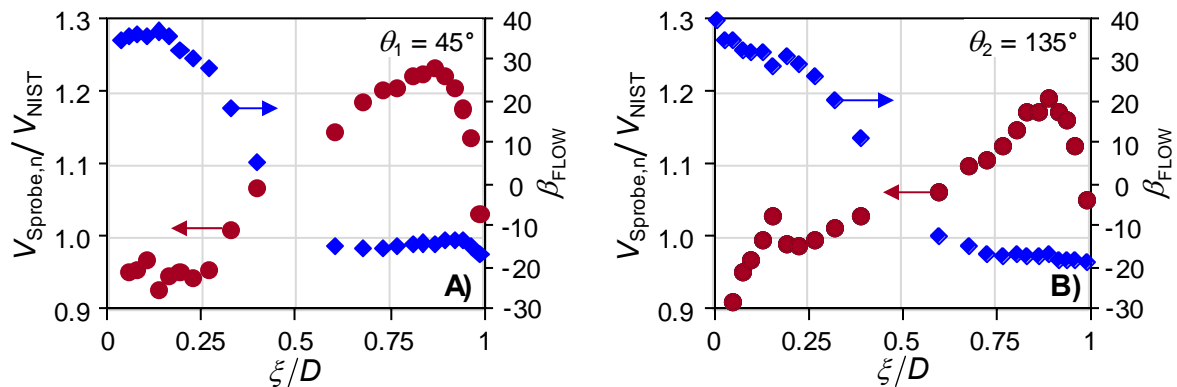


Figure 7. Normalized velocity profile (●) and flow angle (◆) as functions of the dimensionless distance ξ/D along 2 orthogonal chords located 12 diameters ($D = 1.2$ m) downstream from the sharp corner in SMSS. A) 24-point S-probe traverse at $\theta_1 = 45^\circ$, and B) 24-point S-probe traverse $\theta_2 = 135^\circ$.

The results of the S-probe traverse are shown in Fig. 7 where the circles (●) are the normalized velocity profiles and the diamonds (◆) are the flow angle. During the traverse the flow velocity was maintained at $V_{\text{NIST}} = 5.27$ m/s. Figure 7A shows the results for $\theta_1 = 45^\circ$ and Fig. 7B shows the results for $\theta_2 = 135^\circ$. The axial velocity profiles are both skewed toward the outer pipe wall; however, the skew exhibited on the velocity profile at $\theta_1 = 45^\circ$ is slightly more pronounced. The sharp decrease in velocity near the inner and outer walls indicate the thickness of the boundary layer. The cross-flow velocity in the SMSS Test Section is substantial as indicated by the flow angle ranging from near 40° at the inner wall to almost -20° at the outer wall in both orientations.

5.2 S-probe RATA in the SMSS

With the traverse system installed at $z = 12 D$ we assessed the accuracy of an S-probe RATA on 2 diametric chords oriented at $\theta_1 = 45^\circ$ and $\theta_2 = 135^\circ$. We followed the common RATA protocol that uses the value $C_p = 0.84$ for the S-probe calibration factor. The RATA was done at two flow velocities: 5.28 m/s and 23.29 m/s. These velocities approximate low and high loads in a CFPP. At each flow, we conducted a 12-point RATA, a 24-point RATA, and a 48-point RATA. On each chord, the traversing system moved the S-probe radially to the specified RATA point and performed the yaw-nulling procedure described in Section 3 to find $\beta_{\text{FLOW},n}$. The axial velocity at each point was calculated using Eq. (3) and the flow velocity was calculated using Eq. (2). The results are shown in Table 1.

At both the high and low loads, the S-probe RATA overpredicted the actual flow in the SMSS. The largest error of 6.1% occurred at the low load for the 12-point RATA. The modest improvements for the 24-point and 48-point RATA probably resulted from improved resolution of the sharp velocity gradient in the boundary layer close to the wall. The conventional value ($C_p = 0.84$) of the S-probe calibration factor may be too large; if so, it is partly responsible for overpredicting the actual flow velocity. We suspect that significant levels of pitch, which could not be measured with the S-probe, also contribute to the overprediction. Independent of the causes, the overprediction suggests that the quantity of hazardous emissions from actual CFPPs might be significantly overestimated; however, this suggestion must be tested in actual

CFPP stacks by comparing conventional RATA measurements with rigorous measurements traceable to flow standards.

Table 1. S-probe flow RATA performed 12 D downstream of the sharp corner in SMSS facility. Measurements taken by traversing S-probe along orthogonal chords oriented at $\theta_1 = 45^\circ$ and $\theta_2 = 135^\circ$ at low and high loads with $C_p = 0.84$.

No. of Points []	V_{NIST} [m/s]	V_{Sprobe} [m/s]	$100 \left[\frac{V_{Sprobe}}{V_{NIST}} - 1 \right]$ [%]
12	5.28	5.6	+6.1
24	5.28	5.57	+5.5
48	5.28	5.53	+4.7
12	23.29	24.83	+6.6
24	23.29	24.68	+6.0
48	23.29	24.47	+5.1

5.3 Single-Path and X-Pattern CEMS in the SMSS

We assessed the accuracy of the 3 single-path USMs shown in Fig. 5 and an X-Pattern design comprising paths 2 and 3 together. Unlike industrial CEMS applications, we did not calibrate the USMs *via* the RATA. Instead we computed the flow velocities using only the raw meter transit times t_a and t_w along with the dimensionally measured path length (L_p) and path angle (φ). First we calculated the path velocity ($\bar{V}_{USM,p}$) using Eq. (4), and then divided it by $\cos(\varphi)$, as specified by Eq. (1) to determine the flow velocity ($\bar{V}_{USM,f}$). For the X-pattern we computed the flow velocity by averaging the flow velocities from USM 2 and 3, $\bar{V}_{USMx,f} = (\bar{V}_{USM2,f} + \bar{V}_{USM3,f})/2$. The accuracy was assessed by comparing the respective USM flow velocities to the NIST traceable average velocity (V_{NIST}).

The results for the 3 single-path USMs and the X-pattern are shown in Fig. 8. The normalized flow velocity ($\bar{V}_{USM,f} / V_{NIST}$) is plotted against V_{NIST} . Ideally, the normalized flow velocity would be unity, indicating that the USM is not affected by swirl or profile distortions. All three single-path USMs showed substantial biases. USM 1 denoted by the triangles (\blacktriangle) was biased by nearly 6 % over the entire flow range. USM 2 indicated by the diamonds (\blacklozenge) was also biased high, but it had a larger error ranging from 14 % to 17 % depending on flow. In contrast, USM 3 denoted by the squares (\blacksquare) was biased low by 14 % to 17 %. Based on the approximate swirl compensation of the X-pattern design (see Section 4.2) we were not surprised that the biases of USM 2 and 3 had opposite signs. However, we were surprised at the remarkable agreement between the X-pattern denoted by the circles (\bullet) and V_{NIST} . Over the entire range of flow the agreement was better than 0.5 %. This sub-one-percent agreement was unexpected because the X-pattern compensates for swirl, but it does not compensate for profile errors. More testing is required to assess the sensitivity of this result to the installation angle (θ), and to different flow installations. Nevertheless, these initial results indicate that the X-pattern USM is significantly more accurate than a single-path USM.

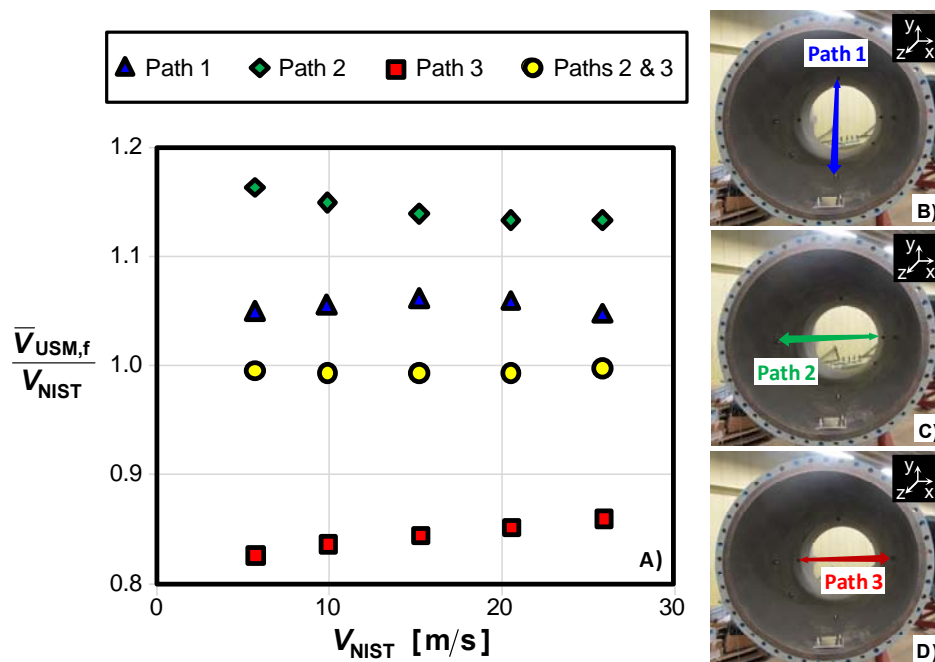


Figure 8. Data comparing the accuracy of 3 single-path USMs versus an X-pattern design. A) plot of USM flow velocity normalized by V_{NIST} , B) orientation of path 1, C) orientation of path 2, and D) orientation of path 3. (Note that paths 2 and 3 together comprise the X-pattern USM).

6 Conclusions

We used the SMSS to generate a known flow (V_{NIST}) with an uncertainty of 0.7 % (at 95 % confidence level) with swirl and profile asymmetry in its $D = 1.2$ m Test Section. The axial velocity and yaw angle along two diametric chords showed that the velocity was ~ 30 % larger on one side of the Test Section than the other. Cross-flow was substantial; the yaw angle varied from $\sim 40^\circ$ on one side of a chord to -20° on the other side. This complex velocity field simulates high-distortion flow condition in a CFPP stack.

In SMSS Test Section, we determined the flow using an S-probe RATA, three single-path USMs oriented at a different installation angles, and an X-pattern USM. A 12-point S-probe RATA overpredicted the actual flow velocity (V_{NIST}) by as much as 6.1 %. The level of overprediction decreased to 4.7 % upon increasing the number of points to 48. The remaining overprediction is probably a consequence of the S-probe's inability to compensate for non-zero pitch and the default calibration factor of 0.84. To further improve the RATA's accuracy, we recommend replacing S-probes with 3 D probes that measure the entire velocity vector.

The 3 single-path USMs had flow errors ranging from 5 % to 17 % of V_{NIST} depending on the installation angle. In contrast, the X-pattern USM determined flows within 0.5 % of V_{NIST} over the entire flow range. We attribute this remarkable result to the swirl compensation of the X-pattern design. Because the X-pattern does not compensate for velocity profile effects, additional testing

is necessary to understand the sensitivity of the X-pattern to asymmetry. We plan to perform these tests both in the SMSS facility and in a full-scale CFFP stack.

These initial results show that the errors in an S-probe flow RATA can (at least for certain flows) exceed the errors of an X-pattern USM monitor by nearly an order of magnitude. If future research confirms this observation, improved RATAs will require replacing S-probes with more advanced pitot probes that complement the accuracy offered by the X-pattern.

REFERENCES

- [1] Dorko, W. D., Kelley, M. E., and Guenther, F. R., *The NIST Traceable Reference Material Program for Gas Standards*, NIST Special Publication 260-126 Rev 2013, 2015.
- [2] U.S. Environmental Protection Agency. *U. S. EPA Ambient Air Monitoring Protocol Gas Verification Program Annual Report CY 2010*, EPA Publication No. EPA-454/R-11-005, 2011.
- [3] Hatfield, J., Pierce, G., and Beusse, R., *EPA Needs an Oversight Program for Protocol Gases Report No. 09-P-0235*, Sept. 16, 2009.
- [4] Gameson, L., Carney, J., Hodges, J. T., and Guenther, F. R., *Environmental Protection Agency Blind Audit 2013*, Report of Analysis No. 646.03-14-071b, 2015.
- [5] Gameson, L., and Guenther, F. R., *Environmental Protection Agency Blind Audit 2010*, Report of Analysis No. 639.03-11-026a, 2011. NIST Report of Analysis No. 639.03-11-026a, 2011.
- [6] Norfleet, S. K., and Roberson, W. R., *Part 75 CEMS Equipment - What's Everyone Using? A Look at Current Trends in CEMS Providers*, EPRI CEMS Users Group Meeting, San Diego, CA, May 2003.
- [7] Environmental Protection Agency, *40 CFR Part 60 Application Method 1 Traverse Points – Stationary Sources*, Washington D.C., 1996.
- [8] Environmental Protection Agency, *40 CFR Part 60 Application Method 2 Velocity and S-type Pitot*, Washington D.C., 1996.
- [9] Environmental Protection Agency, *40 CFR Part 60 Application Method 2G Stack Gas-Velocity/Volumetric Flow Rate-2D probe*, Washington D.C., 1996.
- [10] Shinder, I. I., Khromchenko, V. B., and Moldover, M. R., *NIST's New 3D Airspeed Calibration Rig, Addresses Turbulent Flow Measurement Challenges*, 9th International Symposium on Fluid Flow Measurement (ISFFM), Washington, DC, U. S., April 2015.
- [11] Norfleet, S. K., Muzio L. J., and Martz T. D., *An Examination of Bias in Method 2 Measurements Under Controlled Non-Axial Flow Conditions*, Report by RMB Consulting and Research, Inc., May 22, 1998.
- [12] Borthwick, R. P., Whetstone, J., Yang, J., and Possolo, A., *Examination of United States Carbon Dioxide Emission Databases*, EPRI CEM User Group, Chicago, IL: June 2011.
- [13] Quick, J. C., *Carbon dioxide emission tallies for 210 U.S. coal-fired power plants: A comparison of two accounting methods*, Journal of the Air & Waste Management Association, January 2014.

-
- [14] Johnson, A. N., Boyd, J., Harman, E., Khalil, M., Ricker, J. E., Crowley, C. J., Bryant, R. A.; and Shinder, I. I., ***Design and Capabilities of NISTs Scale-Model Smokestack Simulator (SMSS)***, 9th International Symposium on Fluid Flow Measurement (ISFFM), Arlington, VA, US, April 2015.
- [15] Johnson, A. N., Harman, E., and Boyd, J. T., ***Blow-Down Calibration of a Large 8 Path Ultrasonic Flow Meter under Quasi-Steady Flow Conditions***, The 16th International Flow Measurement Conference FLOMEKO 2013, Paris France, September 2013.
- [16] Brown, G. J., Freund, W. R., and McLachlan, A., ***Testing of an 8-Path Ultrasonic Meter to International Standards with and without Flow Conditioning***, AGA Operations Conference, Orlando, FL, May 21 - 24, 2013.
- [17] Brown, G. J., Augenstein D. R., Cousins, T., ***8-Path Ultrasonic Master Meter for Oil Custody Transfer***, XVIII IMEKO World Congress Metrology for a Sustainable Development, Rio de Janeiro, Brazil, September, 17 - 22, 2006.
- [18] Cimbala, J., and Cengel, Y. A., ***Fluid Mechanics: Fundamentals and Applications***, McGraw-Hill series in mechanical engineering, 2006.
- [19] Jaeger, K. B. and Davis, R. S., ***A Primer for Mass Metrology, National Bureau of Standards (U.S.), Special Publication 700-1***, Industrial Measurement Series. 1987: 79.
- [20] Drenthen, J. G., Kurth M., Hollander H., Vermeulen, M., ***Reducing installation effects on ultrasonic flow meters***, 7th International Symposium on Fluid Flow Measurement (ISFFM), Anchorage, AK, August 12-14, 2009.
- [21] Mattingly, G. E. and Yeh, T. T., ***Effects of pipe elbows and tube bundles on selected types of flowmeters***, Flow Measurement and Instrumentation, Vol. 2, Number 1, p. 4, 1991.
- [22] Mattingly, G. E. and Yeh, T. T., ***Summary Report of NIST's Industry-Government Consortium Research Program on Flowmeter Installation Effects with Emphasis on the Research Period November 1988 to May 1989***, U.S. Department of Commerce, NISTIR 4310, 1989.
- [23] Brown, G. J., and Freund, W. R., and McLachlan, A., ***Analysis of Diagnostic Data from an 8-Path Ultrasonic Meter Testing of an 8-Path Ultrasonic Meter***, AGA Operations Conference, Orlando, FL, May 21 – 24, 2013.
- [24] Zhang, L., Heming, H., Tao, M., and Chi., W., ***Effect of Flow Disturbance on Multi-path Ultrasonic Flowmeters***, FLOMEKO, Paris, France, September 24-26, 2013.
- [25] Brown, G., and Coull, C., and Barton, N., ***Installation Effect on Ultrasonic Flowmeters and Evaluation of Computation Fluid Dynamics Prediction Methods***, 4th International South East Asia Hydrocarbon Flow Measurement Workshop, Kuala Lumpur, Malaysia, March 9–11 2005.